# Electric conversion treatment of cobalt-containing wastewater

Shengnan Lin, Xijuan Pan, Deliang Meng and Tingan Zhang

## ABSTRACT

Long-term accumulation of cobalt-containing wastewater may also pollute groundwater and cause a large amount of loss of valuable metals. Therefore, the comprehensive utilization of cobalt-containing wastewater must be realized, especially as cobalt itself is a very important strategic resource. This paper proposes a membrane electroconversion method to separate cobalt ions from cobalt-containing wastewater and prepare cobalt hydroxide. In addition, the electrolysis process was optimized, and single-factor experiments such as the initial concentration, cobalt ions, current density, temperature etc., and economic calculations such as current efficiency were explored. The electrolysis product was calcined as the precursor to obtain the oxide $Co_3O_4$, and the calcination experiment was also optimized. In this concentration range, more than 90% of cobalt can be recovered within 2 h.

**Key words** | $Co(OH)_2$, $Co_3O_4$, membrane electrolysis, wastewater

**Shengnan Lin**
**Xijuan Pan**
**Deliang Meng**
**Tingan Zhang** (corresponding author)
Special Metallurgy and Process Engineering Institute, School of Metallurgy,
Northeastern University,
Shenyang 110819,
China
E-mail: *zta2000@163.net*

**Tingan Zhang**
Key Laboratory of Ecological Metallurgy of Multi-metal Intergrown Ores of Education Ministry,
Shenyang 110819,
China

## HIGHLIGHTS

- In this paper, a self-made two-chamber electrolytic cell was used to treat wastewater to prepare cobalt hydroxide, and the electrolysis product was used as a precursor for calcination to produce $Co_3O_4$.
- A single-factor experiment was used to investigate its influence. $Co_3O_4$ calcined products, and their microscopic morphology inherited the nanosheet structure of cobalt hydroxide.

## INTRODUCTION

Cobalt production industries produce a large amount of $Co^{2+}$-containing wastewater during the production process, which not only results in serious pollution to the environment, but also causes a large amount of loss of valuable metals. Compounds containing cobalt are difficult to degrade naturally into harmless substances, and cobalt is extremely harmful to aquatic animals. The main domestic production process of basic cobalt carbonate is to obtain basic cobalt carbonate slurry through the substitution reaction of soluble cobalt salt (cobalt chloride or cobalt sulfate) and sodium carbonate solution. After multiple washings to remove impurity ions, and drying to obtain a basic cobalt carbonate product, the washing wastewater contains a large amount of $Co^{2+}$. Lithium battery factories mainly use lithium cobalt oxide and graphite as the positive and negative electrodes, and use the electrolyte as the medium and auxiliary materials to produce lithium batteries (Apiratikul & Pavasant 2008; Karate & Marathe 2008). The wastewater from the battery factory contains a large amount of heavy metal cobalt. Therefore, seeking an economical and efficient treatment process to increase the recovery rate of valuable metals and reduce environmental pollution is an urgent scientific research area for cobalt production industries in the production process.



doi: 10.2166/wst.2021.101

At present, the treatment methods of cobalt-containing wastewater mainly include chemical precipitation, physical chemistry, and biological methods. The chemical precipitation method uses hydroxides, sulfides, etc. to precipitate cobalt to separate cobalt from water (Cavaco *et al.* 2007; Lee *et al.* 2009; Foroutan *et al.* 2017). The treatment effect of this method is limited, and the cobalt content of the effluent often exceeds standards. Biological methods are suitable for low-concentration cobalt-containing wastewater, and rely more on the screening and culture of high-efficiency bacterial flora. Flora are difficult to treat, and are very sensitive to water quality changes, and the application of this technology is rare (Joss *et al.* 2006). Physical and chemical methods, including adsorption, membrane separation and ion exchange resin methods, can not only meet the processing requirements, but also recover the valuable metal cobalt, this approach is a hot research topic in China and elsewhere. Membrane separation is a physical separation process in which water molecules and ions under pressure pass through membranes with different pore sizes; the sieving effect of the membrane pore size achieves separation (Chiu & Chen 2017). The membrane separation method has the characteristics of no phase change, no pollution, and operation at room temperature (Metz *et al.* 2015). The ion-exchange method is to selectively remove certain ions through ion exchange during contact between ion-exchange resin and wastewater, and is suitable for low-concentration wastewater. The ion-exchange method has the characteristics of simple operation, good treatment effect, etc., and it is easy to realize automation, and therefore a promising technology (Xie *et al.* 2014). Due to its large specific surface area, mesoporous cobalt tetroxide has good optical, electrical and chemical properties, and is widely used in supercapacitors (Meher & Rao 2011; Xia *et al.* 2011; Liu *et al.* 2018), cemented carbide (Takahashi & Fine 1972), lithium battery electrode materials (Lou *et al.* 2007; Wang *et al.* 2010; Liao *et al.* 2013; Yu 2013), adsorbents (Yavuz *et al.* 2013), inorganic pigments (Yoneda *et al.* 2019), magnetic materials (Chaturvedi *et al.* 2015) and catalysts (Tüysüz *et al.* 2008; Liang *et al.* 2011; Xu *et al.* 2012) and other fields. Among them, mesoporous cobalt tetroxide is particularly attractive as an electrocatalytic oxidation catalyst for water.

In this paper, the cobalt-containing wastewater from a certain company was used as the treatment object. First, a self-made two-chamber electrolyzer was used to conduct membrane electrolysis experiments, and cobalt hydroxide was successfully recovered from the wastewater and prepared. Secondly, the influence of different single factors on the electrolysis products in the process of membrane electrolysis was investigated. Finally, cobalt hydroxide was used as a precursor to calcination to obtain high-purity cobalt tetroxide. At the same time, the effects of calcination temperature and time on $Co_3O_4$ were investigated.

## EXPERIMENTAL SECTION

### Experimental materials and homemade electrolyzer

The cobalt-containing wastewater produced by a domestic company in the production process was used. The approximate value of the wastewater composition is shown in Table 1. Cationic film (CJMC-3) purchased from Hefei Chemical Joy Polymer Materials Co., Ltd.

### Membrane electrolysis process

This study used industrial cobalt-containing wastewater as the anode solution for the electrolysis experiment (Figure 1), and investigated the influence of electrolyte concentration, temperature, current density, different surfactants, external stirring, and ultrasonic vibration on the electrolysis process. Then, the optimized concentration of magnesium chloride was used as the anolyte, and the cobalt hydroxide precipitated at the cathode was calcined, and the influence of the calcination temperature and time of the oxide was investigated. The whole electrolysis reaction process consisted of three steps. First, the bipolar reaction. The anode generates chlorine gas and the cathode generates hydrogen; then $Co^{2+}$ migrates from the anode to the cathode under the

**Table 1** | Composition of cobalt-containing wastewater

| Composition | $CO_3^{2-}$ | $Co^{2+}$(mg/L) | $Cl^-$ | $NH_4^+$ |
|---|---|---|---|---|
| Content g/L | 20 | 100 | 50 | 21 |

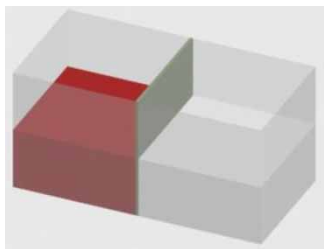

**Figure 1** | Schematic diagram of self-made two-chamber electrolyzer.

action of current and concentration; finally, $Co^{2+}$ and the $OH^-$ near the cathode electrode precipitate (Dang *et al.* 2007; Narbaitz *et al.* 2013; Pan *et al.* 2020). The reaction equation of the membrane electrolysis process is as follows:

Anode reaction: $Cl^- - 2e \rightarrow Cl_2\uparrow$

Cathodic reaction: $H^+ + 2e \rightarrow H_2\uparrow$

Precipitation process: $Co^{2+} + 2OH^- \rightarrow Co(OH)_2\downarrow$

Total reaction equation: $CoCl_2 + 2H_2O \rightarrow Co(OH)_2\downarrow + Cl_2\uparrow + H_2\uparrow$

After the electrolysis experiment had completed, the pink precipitate was collected and filtered at the cathode, then washed with deionized water and alcohol three times each, and then dried at 60 °C for 12 hours.

### Calculation method

In this article, the economic standards for measuring the ion-exchange membrane electrolysis process mainly include current efficiency, DC power consumption and productivity:

$$\eta = \frac{m_{actual}}{m_{theoretical}} \times 100\% = \frac{m_{actual}}{I \times \Delta t \times M/(n \times F)} \times 100\% \quad (1)$$

Among them, $\eta$ is the cathode current efficiency, %; $m_{(actual)}$ and $m_{(theoretical)}$ are the mass of the actual cathode product and the mass of the product calculated according to Faraday's law, g; $M$ is the molar mass of the cathode product, g·mol$^{-1}$; $I$ is the current, A; $\Delta t$ is the electrolysis time, s; $F$ is Faraday's constant (about 96,500 C·mol$^{-1}$); and $n$ is the number of electrons passing through the electrode reaction:

$$W = \frac{kV}{\eta} \quad (2)$$

$W$ is the DC power consumption, kW·h·kg$^{-1}$; $\eta$ is the cathode current efficiency, which can be calculated by Equation (2), %; and $V$ is the cell voltage of the electrolysis process. Since this experiment uses constant current electrolysis conditions, the cell voltage in the electrolysis process was not constant, so the expected value of the cell voltage during the electrolysis process was calculated according to the arithmetic average of the cell voltage, V; $k$ is the theoretical power consumption of the electrolysis process, kA·h·kg$^{-1}$.

Theoretical power consumption ($k$) is the theoretical power consumption required to produce a unit mass product. The calculation equation is shown in (3): $k$ is the theoretical power consumption, kA·h·kg$^{-1}$; $Q$ is the amount of charge passed through the electrolysis process, C; $m_{(theoretical)}$ is the mass of the product that should be generated theoretically when the amount of charge $Q$ passes through the electrolysis process, g; $n_A$ is the number of moles of charge passed through the electrolysis process, mol; and $F$ is Faraday's constant (about 96,500 C·mol$^{-1}$):

$$k = \frac{Q}{3600 \cdot m_{theoretical}} = \frac{n_A}{3600 \cdot m_{theoretical}} \quad (3)$$

The productivity of the electrolysis process is the quality of the product produced per unit time. It is an important indicator to measure the production capacity. The specific calculation method is shown in Equation (4):

$$\text{productivity} = \frac{m(actual)}{t} \quad (4)$$

The unit of productivity is g·h$^{-1}$; $m_{(actual)}$ is the actual product quality, g; and t is the electrolysis time, h.

### Material characterization

The structure and chemical analysis of the samples was performed by powder X-ray diffraction (XRD) (CuK$\alpha$ radiation, Bruker D8 Advance, Germany). The surface morphology of the sample was observed using a scanning electron microscope (SEM) (Zeiss Sigma 300). The weight loss of the precursor was analyzed by differential scanning calorimetry-thermogravimetric analysis (DSC-TGA) (SDT Q600 V20.9 Build 20, 10 °C/min).

## RESULTS AND DISCUSSION

### Effect of initial concentration of cobalt ion on product

The X-ray diffraction pattern of the product of different $Co^{2+}$ concentration conditions is shown in Figure 2(a). It can be roughly seen in Figure 2(a) that as the concentration was increased, the crystallinity gradually increases, and the crystallinity is optimal when the cobalt ion concentration is 0.2 mol·L$^{-1}$. (001), (100), (101) and other diffraction peaks are consistent with the standard diffraction peaks of cobalt hydroxide (JCPDS card no. 30-0443), indicating that the prepared sample is hexagonal $\beta$-$Co(OH)_2$ (Tong *et al.* 2017; Youssry *et al.* 2020). All diffraction peaks from XRD can be retrieved for $\beta$-$Co(OH)_2$ hexagonal phase diffraction data (according to standard spectrum JCPDS card no. 30-0443). It can be seen from the different curve images

that the degree of crystallinity gradually increases, and the characteristic peaks become more and more obvious. The high intensity of the (101) diffraction peak indicates that the crystallites of $\beta$-$Co(OH)_2$ have a preferred orientation along the (101) axis during their deposition (Kitahata *et al.* 2000). In particular, no diffraction peaks related to the $\alpha$ phase of cobalt hydroxide were observed. It can be concluded that under the applied cathodic electrodeposition conditions, pure $\beta$-phase cobalt hydroxide can be obtained (Aghazadeh *et al.* 2014). The characteristic peaks are not significantly broadened and refined, and we can infer that the grain size has not changed much (this inference is also confirmed by the scanning electron microscope later).

According to the equation, crystallinity

$$= \frac{1 - \text{all amorphous peak intensities}}{\text{Scattering intensity of 100\% fully amorphous standard}} \times 100\% \quad (5)$$

crystallinity

$$= \frac{\text{Sample crystal diffraction peak intensity}}{\text{Diffraction intensity of 100\% complete crystalline standard}} \times 100\% \quad (6)$$

The calculation formula is simplified, no standard sample is needed, and crystallinity can be calculated from one sample according to Equation (7). The crystallinity of each sample was calculated to be 34.0%, 85.04%, 94.06%, and 99.25%. When the cobalt ion concentration was 0.05 mol/L, the crystallinity of this sample was roughly calculated to be 34.0%, and the crystallinity of this sample was poor. The curves of the latter three concentrations overlapped, indicating that the sample has good crystallinity and can produce stable crystals. As the concentration was increased, the crystallinity also increases. For samples with small to large concentrations, and crystallinity from low to high, it was concluded that the optimal solution concentration for electrodeposition preparation $Co(OH)_2$ was 0.2 mol·$L^{-1}$:

$$\text{Crystallinity} = \frac{\text{Diffraction peak intensity}}{\text{total intensity}} \times 100\% \quad (7)$$

Figure 3 shows the surface morphology of $\beta$-$Co(OH)_2$ powder under different initial concentrations of cobalt ions. The SEM image shows that the prepared deposit has a uniform and clear sheet-like nanoscale structure. As the concentration of cobalt ions was increased, the dispersibility of cobalt hydroxide gradually increases, and the hexagonal flake shape becomes more obvious. According to rough estimation, the particle diameter ranges for small to large cobalt ion concentrations are: (a) 40–107 nm; (b) 50–110 nm; (c) 10–70 nm; (d) 30–85 nm; the thickness is only a few nanometers. The electrodeposited $Co(OH)_2$ has a unique spatially staggered nanosheet network morphology, and the thickness of the nanosheets is uniform with a relatively large specific surface area. Photographs in (a), (b), (c) are not as clear as (d), because

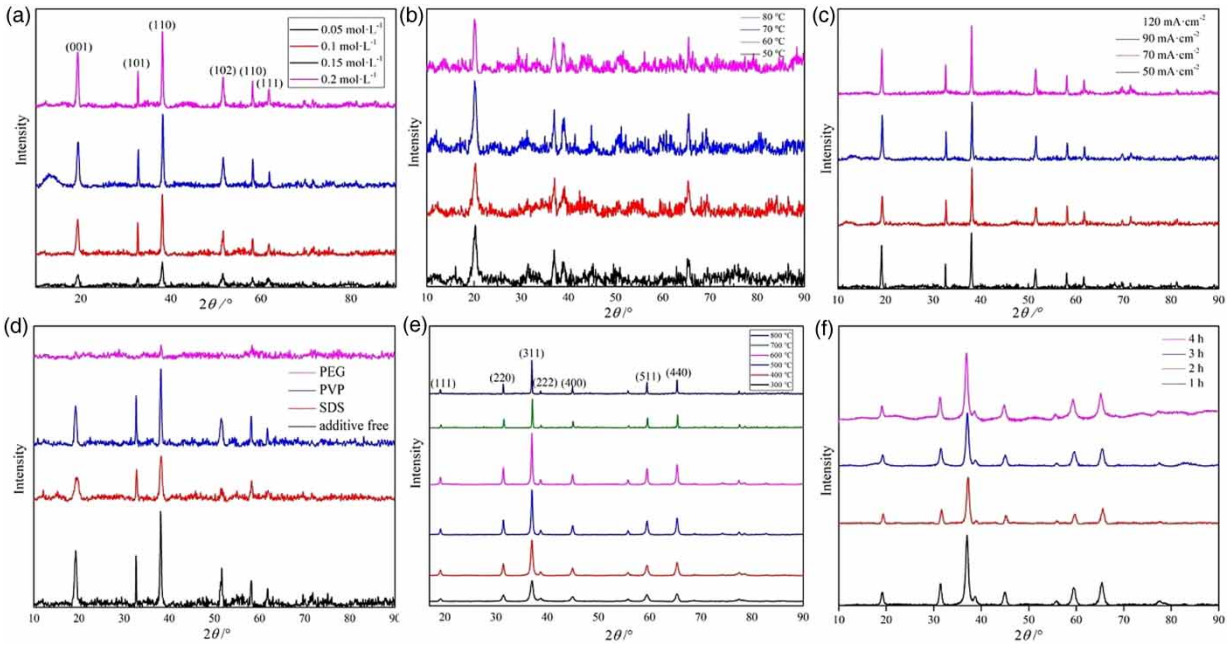


**Figure 2** | XRD image of: (a) different iron ion concentrations; (b) different temperatures; (c) different current densities; (d) no additives and different additives; (e) different stirring rates; (f) different ultrasound frequencies.

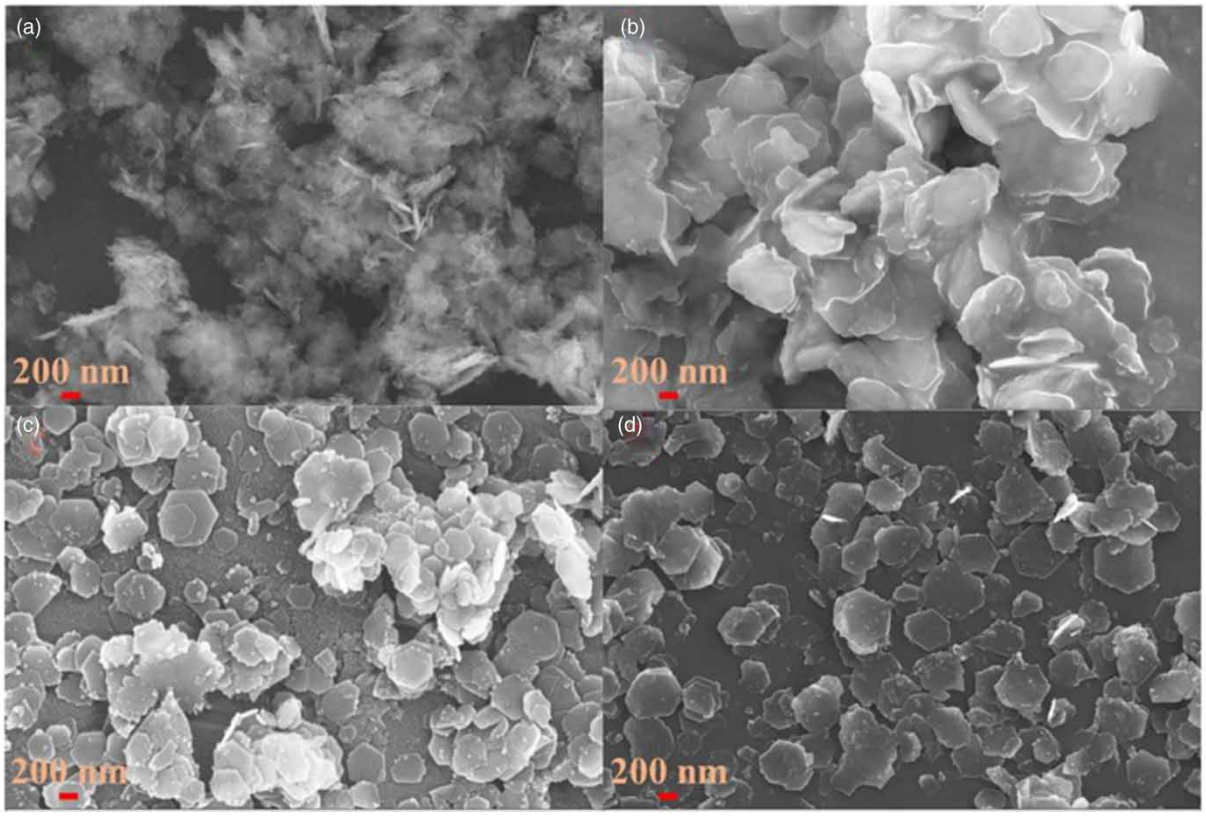


**Figure 3** | SEM pictures of different $Co^{2+}$ concentrations: (a) 0.05 mol·L$^{-1}$; (b) 0.1 mol·L$^{-1}$; (c) 0.15 mol·L$^{-1}$; (d) 0.2 mol·L$^{-1}$.

the sample had been stored for too long, but the hexagonal sheet structure can still be seen. The interlaced nanoflake network morphology makes it produce rapid ion migration in the electrochemical oxidation–reduction reaction, so that the electroactive material can be fully utilized to speed up the reaction. At the same time, it is also conducive to the formation of electric double layers.

## Effect of electrolysis temperature of cobalt ion on product

As shown in Figure 4(a), compared with the room temperature reaction, when the reaction temperature was lower, the viscosity of the electrolyte solution is relatively large, the conductivity is low, and the diffusion is slow, which blocks the conduction of electrons in the solution and the cobalt in the anode chamber to the cathode diffusion process. As the reaction temperature was increased, the viscosity of the electrolyte decreases and the conductivity increases, which can accelerate the diffusion of cobalt ions into the cathode, and at the same time promote the generation of chlorine and hydrogen at the cathode. Conversely, a higher temperature is conducive to the improvement of ion migration rate in the electrolyte solution, resulting in an increase in current efficiency and a decrease in DC power consumption. When the electrolysis temperature is 60 °C, the electrolysis experiment is the best. As shown in Figure 4(b), as the temperature was increased, the cell voltage first decreases and then increases. The increase in temperature reduces the activation energy of the reaction. From a theoretical analysis, this phenomenon conforms to the Arrhenius formula: $k = Ae^{-E_a/RT}$. As the temperature was increased, the activation energy $E_a$ decreases, which can increase the reaction rate constant $k$. The increase in temperature makes the electrode reaction rate of $H_2$, $Cl_2$, $Co(OH)_2$ faster, thus lowering the cell voltage, while the cell voltage at 80 °C increases, indicating that the electrolysis experiment requires a lower temperature increase to meet the market conditions. It can be roughly seen from the XRD curve that the characteristic peak intensity is the largest when the temperature was 70 °C, followed by 50, 80, and 60 °C. The lattice constants of the samples are both $a = 5$ Å and $c = 5$ Å, so each $Co(OH)_2$ has a regular hexagonal crystal structure. According to the simplified calculation Equation (7) of crystallinity, the crystallinity of the sample under different temperature conditions was 100%.

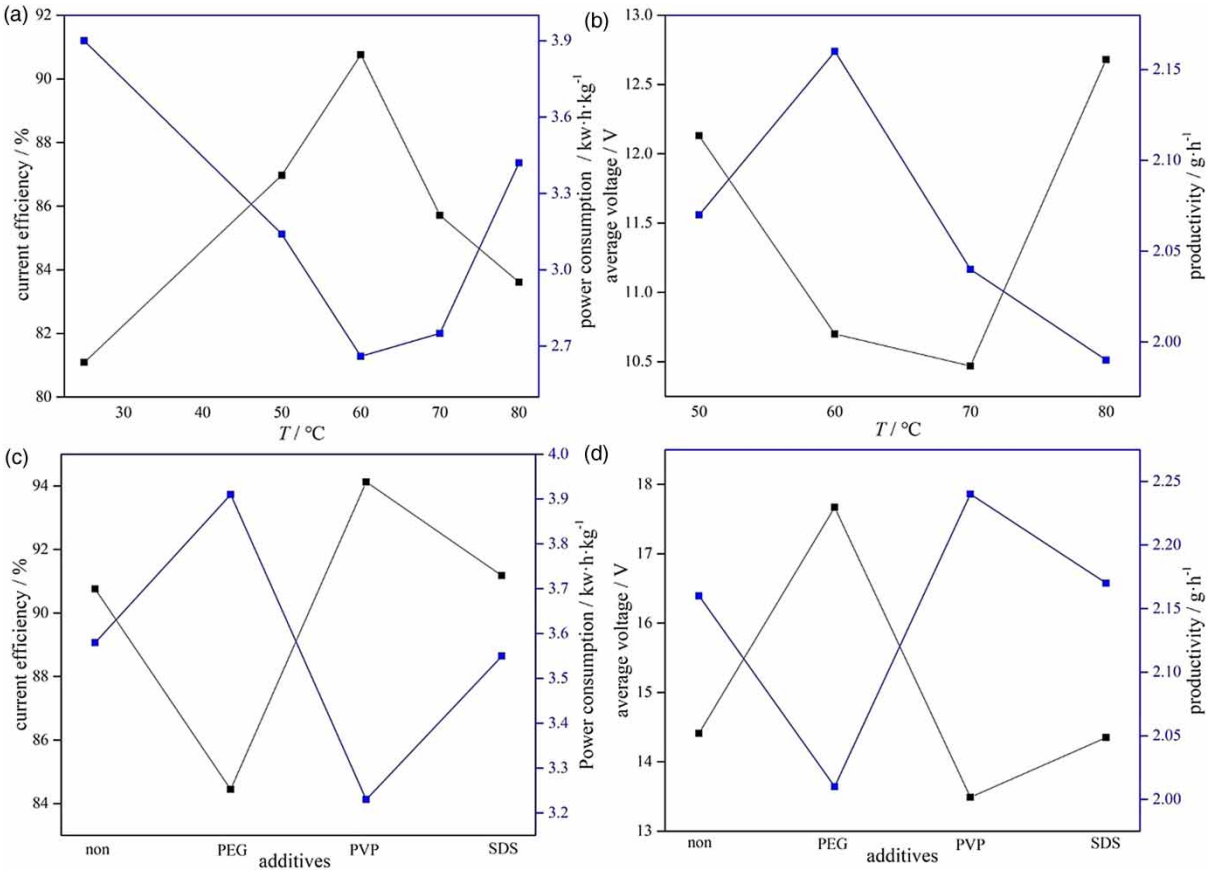


**Figure 4** | (a) Effect of temperature on current efficiency and DC power consumption. (b) Effect of temperature on average voltage and productivity. (c) Effect of additives on current efficiency and DC power consumption. (d) Effect of additives on average voltage and productivity.

From the perspective of crystallinity, when the above different temperatures are set, the crystallinity of the sample can be as high as 100% without an amorphous peak.

Figure 5 shows the surface morphology of $\beta$-$Co(OH)_2$ powder under different temperature conditions. Arranged in descending order of temperature, the particle diameter ranges were: (a) 10–30 nm; (b) 20–70 nm; (c) 20–65 nm; (d) 15–75 nm, but their thickness was only a few nanometers. The powder had flake-like structure that crosses horizontally and vertically. At 50 °C, due to the smaller diameter, more nanoscale pores were formed with the most gaps; at 60 °C, the diameter range becomes larger, and it is still an irregularly cross-layered structure; the flake structure is obvious at 70 °C, and the diameter range becomes smaller than that at 60 °C, and the flakes intersect and agglomerate closely to form a porous structure; at 80 °C, the interlaced structure is obvious, the diameter range is relatively larger, and the crystals are denser.

## Effect of current efficiency

Figure 2(c) shows that with the increase in the current density, the characteristic peaks become sharper and the intensity becomes higher and higher. By comparing with the standard XRD curve, it was found that all peak positions of the prepared $Co(OH)_2$ sample are consistent with the standard sample, and the XRD diffraction peak intensity is high, which proves that the $Co(OH)_2$ prepared by our group had good crystallinity. From the perspective of crystallinity, when the current density was 70 $mA{\cdot}cm^{-2}$ and 120 $mA{\cdot}cm^{-2}$, the crystallinity was as high as 100%. Figure 6 shows the surface morphology of $\beta$-$Co(OH)_2$ powder under different current density conditions. The particle diameter ranges from small to large current density are: (a) 30–120 nm; (b) 30–80 nm; (c) 40–170 nm; and (d) 30–170 nm.

The actual crystallization mechanism of $Co(OH)_2$ is still an open question. At present, initial nucleation, directional

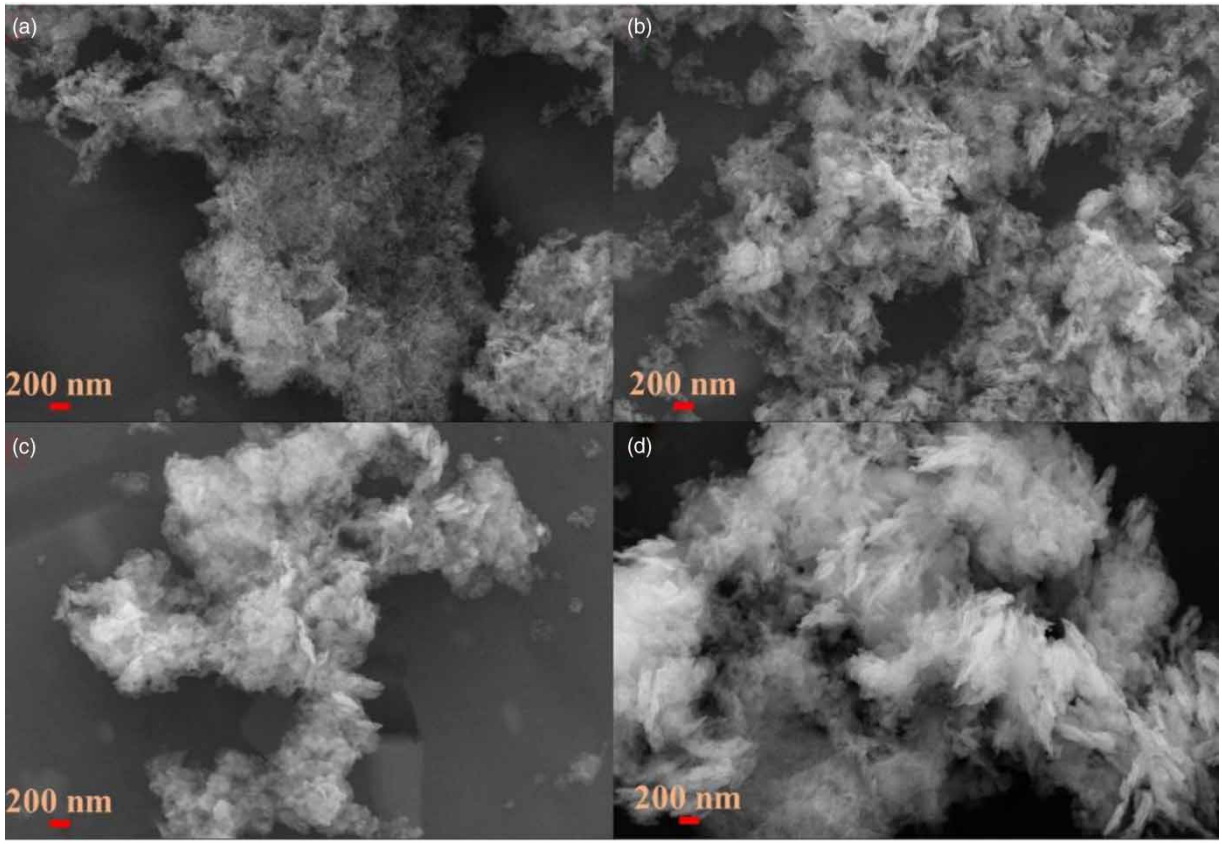


**Figure 5** | SEM pictures under different temperatures: (a) 50 °C; (b) 60 °C; (c) 70 °C; (d) 80 °C.

aggregation and Ostwald ripening can be used to explain the process of crystal growth. The cobalt ion in the aqueous solution reacts with the $OH^-$ generated near the cathode plate to form $Co(OH)_2$, and the reaction is as described in Equation (8):

$$Co^{2+} + OH^- \rightarrow Co(OH)_2 \quad (8)$$

Subsequently, the nanoparticles began to assemble together and spontaneously aggregated into $Co(OH)_2$ nanosheet structures. As the high surface energy is reduced through the process of directional aggregation, layered $Co(OH)_2$ nanosheets are formed (Pacholski *et al.* 2002). Ostwald maturation determines the rate of growth and recrystallization (Li *et al.* 2002), and through the Ostwald maturation process, the smaller $Co(OH)_2$ crystal particles produced in the solution are reduced due to the curvature. Larger, higher energy particles, gradually dissolved into the surrounding electrolyte, and then re-precipitated on the surface of the larger $Co(OH)_2$ crystal particles, which makes the larger $Co(OH)_2$ crystal particles further increase.

## Effect of surfactants

Figure 2(c) shows that by adding a small amount of organic additives during the electrodeposition process, it is easy to obtain a dense product deposition layer. The additives adsorbed on the electrode surface change the structure of the electric double layer, because this adsorption enhances polarization and makes the crystals finer. The adsorption of surface active substances is different for different crystal planes. The growth of crystal planes with strong adsorption of surface substances is hindered, while the development of crystal planes with less adsorption will change the growth morphology of the crystal. The external electric energy activates the ions, and the ions pass through the adsorption layer of the surfactant to discharge. Compared with the addition of complexing agents, the method of adding surfactants to control the electrode process has the advantages of low concentration, low cost, no effect on the chemical properties of metal ions in the solution, easy handling, non-toxic, etc., and is mostly used in the processing industry diaphragm electrodeposition process for wastewater. After adding the additive polyethylene glycol (PEG), the diffraction peak

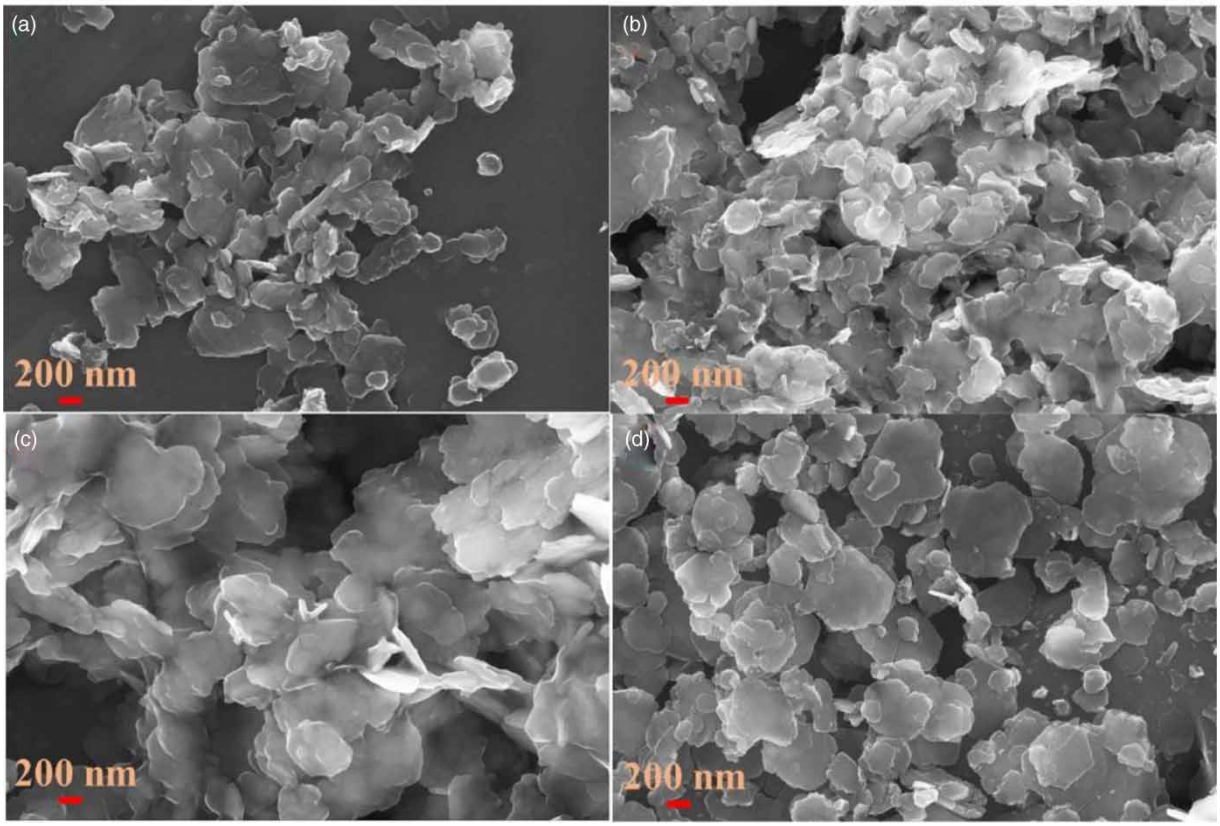


**Figure 6** | SEM of product under different current densities: (a) 50 mA·cm$^{-2}$; (b) 70 mA·cm$^{-2}$; (c) 90 mA·cm$^{-2}$; (d) 120 mA·cm$^{-2}$.

intensity of the sample is significantly reduced, resembling a steamed bread peak, similar to a colloidal structure, which corresponds to the surface micromorphology in Figure 7 below. In the curve comparison with and without additives, it can be seen that without additives, the crystallinity of the product is the highest, followed by the addition of the surfactant polyvinylpyrrolidone (PVP) > sodium dodecyl sulphate (SDS) > polyethylene glycol (PEG). Compared with the XRD curve with SDS, the diffraction peaks of the sample with SDS are obviously broadened and weakened. This shows that the crystallization degree of the sample with SDS added is lower. Therefore, in the experiment of preparing cobalt hydroxide by diaphragm electrolysis, the addition of surfactants reduced the crystallinity of the sample, and even changed from crystal to colloidal. The electrolytic preparation of the surfactant-free diaphragm is an obvious advantage over other preparation methods.

The addition of surfactant PVP is beneficial to improve current efficiency, reduce cell voltage, increase productivity, and reduce DC power consumption. However, the main reason why the output of the surfactant PVP is higher than that of no additives is the extra weight of the additives. The effects of other additives, PEG and SDS, are far inferior to those without additives, and the best additive PVP produces the same effect as without additives. From an economical point of view, the experimental results without additional surfactants are the best.

Additives such as PVP, SDS and PEG will not chemically react with the electrolytic solution, and no new crystal nuclei are generated to affect the growth of the original crystal nucleus. It can be observed that the difference between the surface morphology of the product when different organic solvents is added is very small, which means that different organic solvent additives affect the morphology of $Co(OH)_2$ particles by affecting the way of crystal nucleus agglomeration. Some inert organic macromolecular additives are added in the initial stage of electrolytic preparation. Although they do not participate in the reaction, the additives have a steric hindrance effect on the aggregation of atoms. As far as the current research is concerned, the steric hindrance effect is helpful in preventing the anisotropic growth of the crystal grains, and can maintain the flake shape into the final shape. Although its influence on the grain growth mechanism is not fully understood, the particle shape can still be

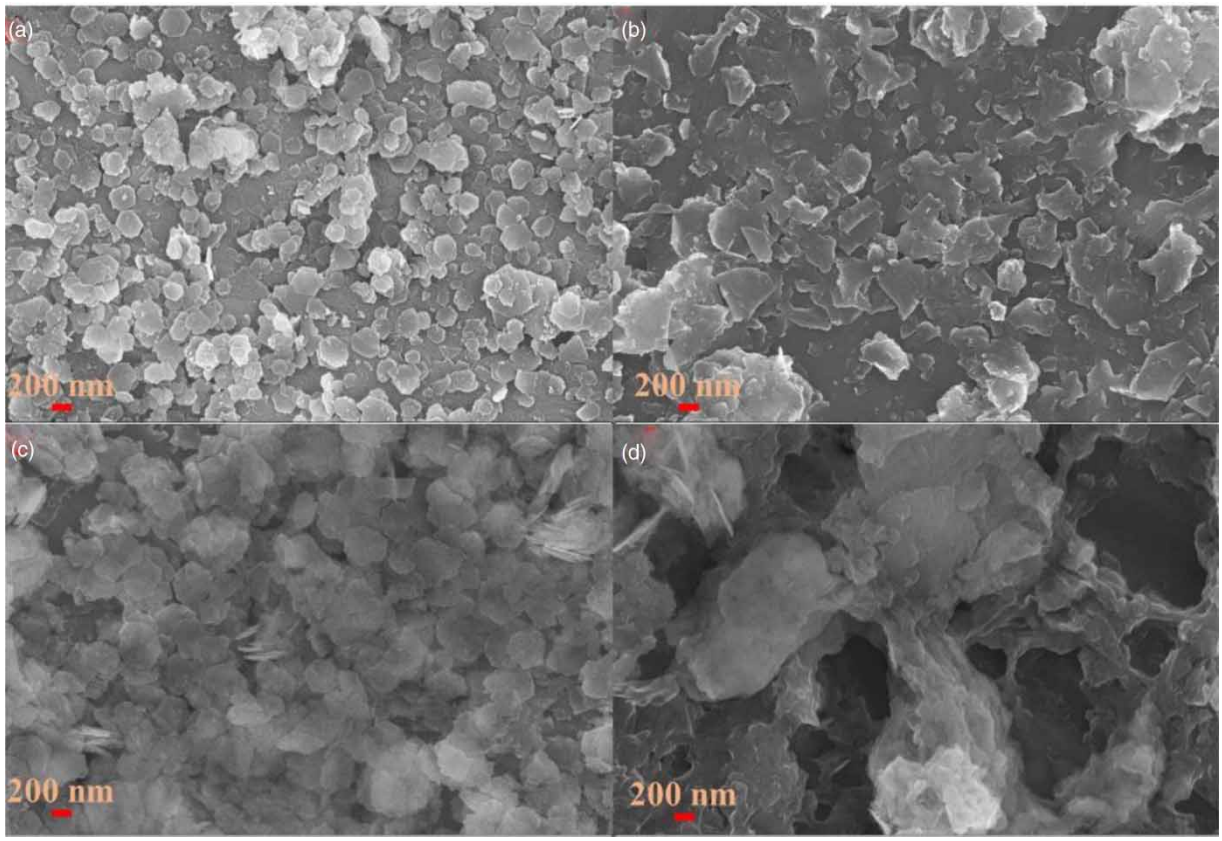


**Figure 7** | SEM of products under no additives and different additives: (a) no additives; (b) PEG 1 g·L$^{-1}$; (c) PVP 1 g·L$^{-1}$; (d) SDS 1 g·L$^{-1}$.

controlled. Three different surfactants all provide different force field environments for the growth of $Co(OH)_2$, and finally form tiny morphological differences. In terms of morphology, it is uneconomical for the addition of surfactants to destroy the original hexagonal structure.

## $Co(OH)_2$ as a precursor

Figure 8 shows the DSC-TGA curve of the $\beta$-$Co(OH)_2$ sample by adding a surfactant PVP. Figure 8 shows that the TGA curve loses 3% at 30–158 °C, and the weight loss in this range is attributed to the sample adsorption water desorption. The maximum weight loss occurs at 158 °C, and this weight loss extends to 615 °C. When the temperature reaches 242 °C, the weight loss reaches 27%, which is caused by the dehydration of water and the decomposition of some anions $CO_3^{2-}$ and the oxidation of $Cl^-$ due to the dehydroxylation of hydroxide. The weight loss here corresponds to an endothermic peak at about 242 °C on the DSC curve, and there may be oxidation of $Co^{2+}$. The decrease in mass at 242–557 °C is attributed to the combustion reaction of surfactant PVP, which indicates that it is not economical to prepare Co for surfactant addition if it is necessary to calcinate Co to oxide. When the temperature exceeds 557 °C, the TGA curve tends to be substantially stable, indicating that the adsorbed impurities in the sample have completely decomposed.

## Effect of calcination temperature

The product is single in the calcination temperature range of 300–800 °C, and the X-ray diffraction peak is sharp and fine, indicating that the calcination product has good crystallinity. When the calcination temperature is 300 °C, there was no need to increase the temperature, which greatly saves energy consumption. The diffraction peaks are approximately $2\theta = 19°$, 31°, 37°, 45°, 59°, 66°, corresponding to (111), (220), (311), (222), (400), (422), (511), (440) crystal planes, corresponding to the literature value (Liao *et al.* 2015), the standard card (JCPDS card no. 42-1467) determines that the $Co_3O_4$ produced after calcination is a cubic crystal system. As the calcination temperature continues to increase, the diffraction peaks become sharper and the particle size of $Co_3O_4$ increases. As the temperature

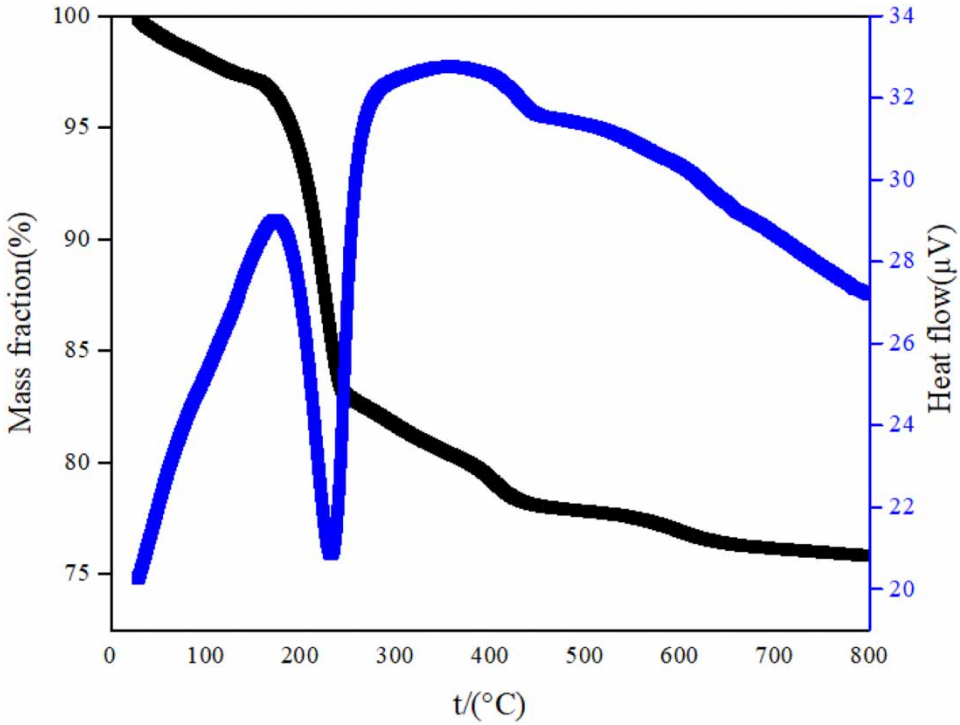


**Figure 8** | DSC-TGA diagram of $Co(OH)_2$.

decreases, the diffraction peak of $Co_3O_4$ broadens significantly, indicating that the $Co_3O_4$ particles produced are smaller (He *et al.* 2005).

As shown in Figure 9, $Co_3O_4$ has a sheet-like structure similar to $Co(OH)_2$, but the surface of $Co_3O_4$ is rougher and there are a large number of pore structures due to the thermal decomposition of $Co(OH)_2$ to produce $O_2$ and $H_2O$ (Ghosh *et al.* 2013). The particle size of $Co_3O_4$ is approximately (a) 45–104 nm in diameter, 4–11 nm in thickness; (b) 34–96 nm, 5–10 nm in thickness; (c) 30–65 nm, 3–7 nm in thickness; (d) 20–110 nm, 4–10 nm thick; (e) 20–115 nm, 4–20 nm thick; (f) 20–135 nm, 4–12 nm thick. This shows that the higher the calcination temperature, the larger the particle size. The interlaced pores formed by the sintering flakes easily penetrate the electrolyte and can increase the contact area between the electrolyte ions and the electrode material. The diameter of the pores formed by cross-linking of the nanosheets is about 12 nm. These pores make it easy for the electrolyte to penetrate, which is beneficial to improve the utilization of the active sites of the electrode material, and is beneficial to the transport of electrolyte in electrochemical reactions. The thickness of the nanosheet was about 10–20 nm, and the thinner sheet structure can provide more active sites per unit mass of active material (Maile *et al.* 2009).

### Effect of calcination time

The calcination time had no obvious effect on the crystallinity and surface morphology of the material (Figures 2(f) and 10). When the calcination time is 1 h, the diffraction peak of the oxide $Co_3O_4$ is the sharpest. When the calcination time is increased, the intensity of the diffraction peak does not increase or even begins to weaken, indicating that a shorter calcination time can reach a certain degree of crystallinity. The samples calcined at different times showed hexagonal flake morphology similar to its precursor cobalt hydroxide, indicating that the calcined product better inherited the morphological characteristics of the precursor, but compared with the precursor $Co(OH)_2$. The particle size of $Co_3O_4$ is larger, and the thickness also increases, around 6–20 nm. The growth of crystal grains on the sample surface is scattered, and the surface morphology is relatively flat. The surface of the sample is smooth, the surface particles are very small, and the agglomeration of small crystal grains is obvious.

## CONCLUSION

In this study, a self-made two-chamber electrolyzer was used to investigate the influence of the initial

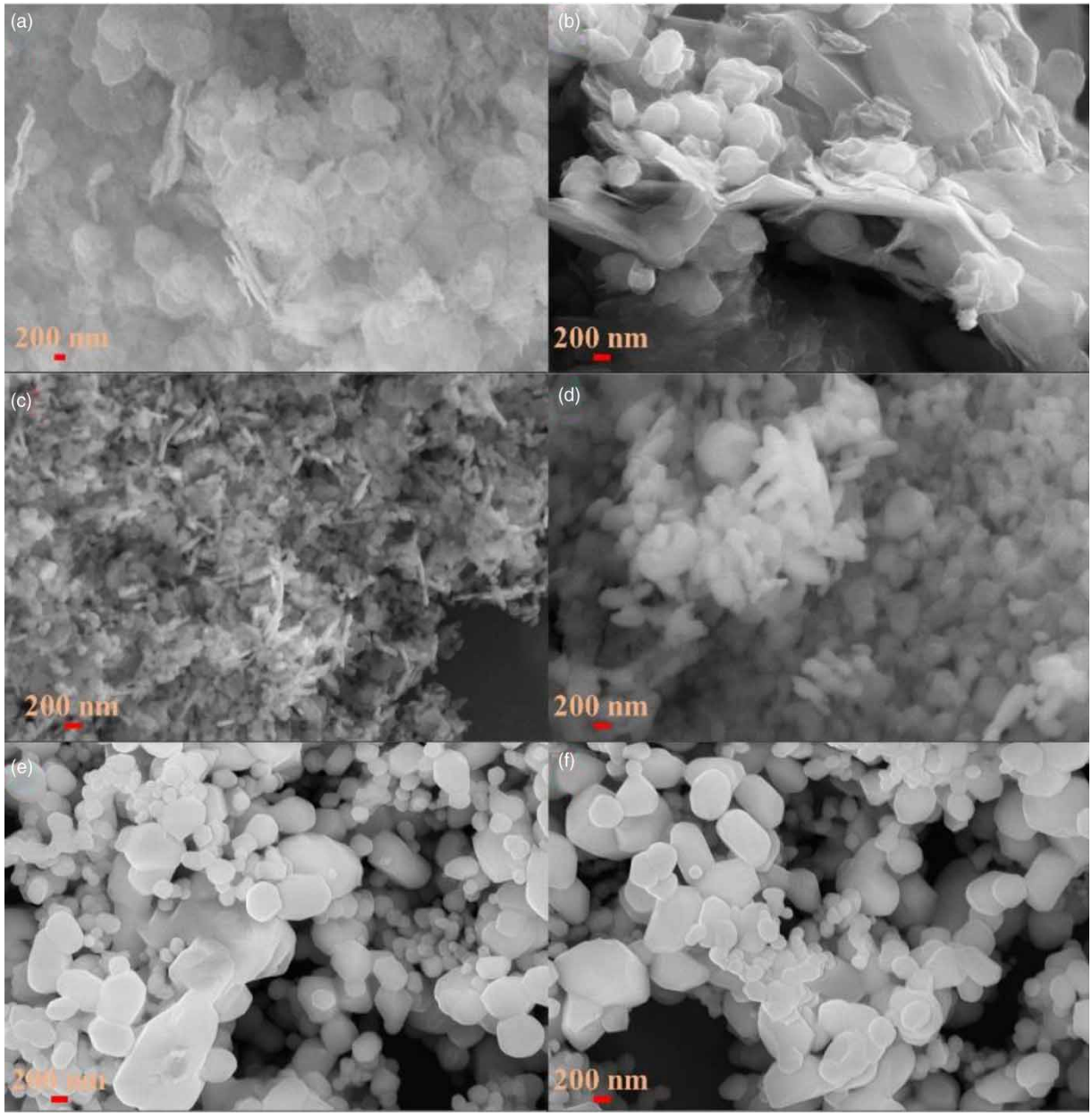


**Figure 9** | SEM images of electrolysis products at different calcination temperatures: (a) 300 °C; (b) 400 °C; (c) 500 °C; (d) 600 °C; (e) 700 °C; (f) 900 °C.

concentration, current density, reaction temperature, and additives on the electrolytic conversion process. The results show that the best electrolysis process conditions are: current density 500 $A \cdot m^{-2}$, the initial reaction temperature is 60 °C, the $CoCl_2$ concentration is 0.2 $mol \cdot L^{-1}$, and there is no additive. The prepared sample is a layered $\beta$-$Co(OH)_2$ nanosheet with hexagonal crystal phase. In the experiment to prepare cobalt hydroxide by diaphragm electrolysis, the addition of surfactant reduced the crystallinity of the sample, and even changed it from crystal to gel. The electrolysis preparation of diaphragm without surfactant is a clear advantage over other preparation methods. The precipitate obtained by electrolytic conversion was studied by calcination experiment, and the influence of calcination temperature and time on the product was investigated. The precipitated products obtained by electrolytic conversion are all calcined $Co_3O_4$, and their microscopic morphology inherited the

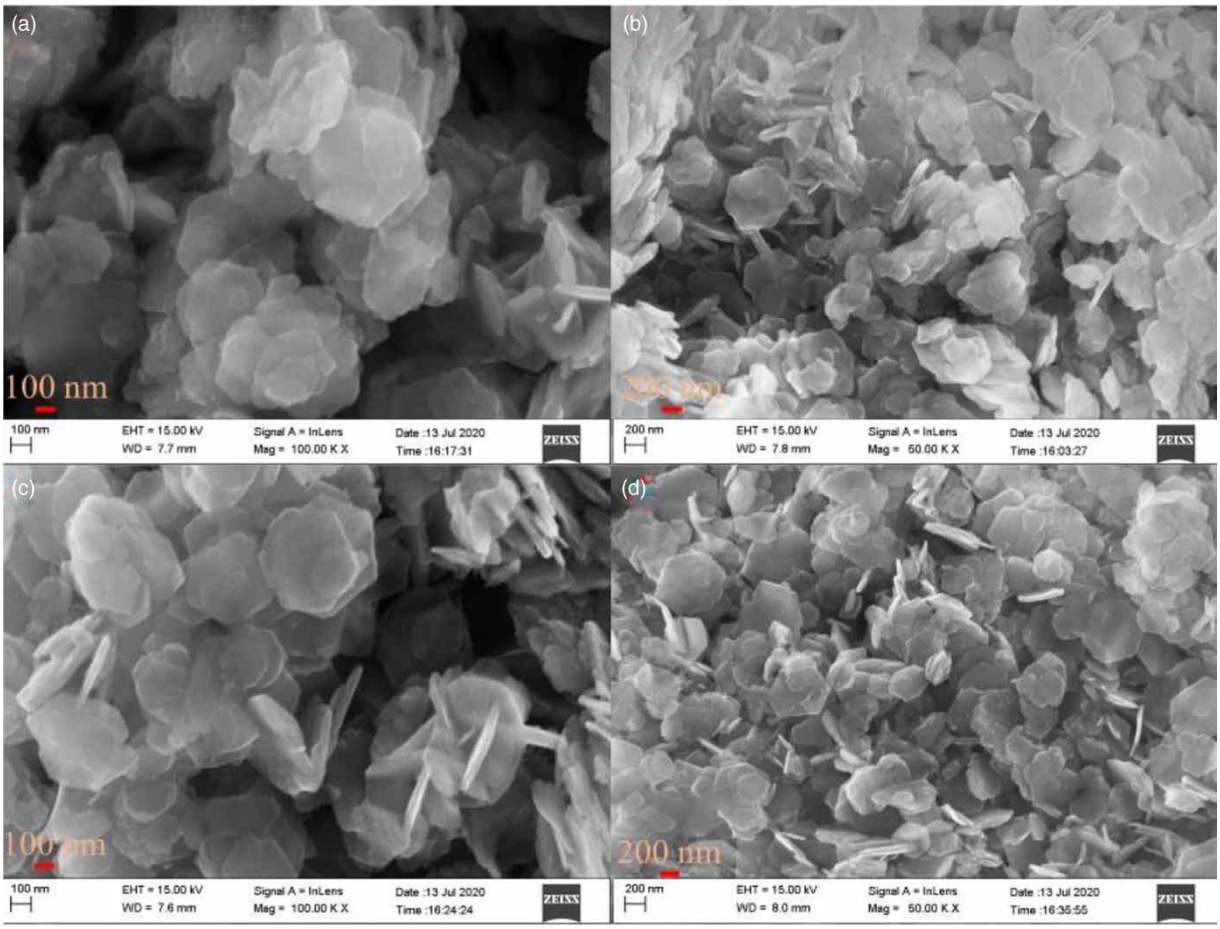


**Figure 10** | SEM images of electrolysis products at different calcination durations.

nanoplate structure of cobalt hydroxide. The pores formed by cross-linking between the nanosheets make it easy for electrolyte to penetrate, which is beneficial to improve the utilization of the active sites of the electrode material. The thickness of the nanosheet was about 10–20 nm, and the thinner sheet structure can provide more active sites per unit mass of active material. The best calcination temperature for electrolytic conversion precipitated product was 300 °C, and the calcination time was 1 h. The products $Co(OH)_2$ and $Co_3O_4$ can be used as catalysts for water electrolysis.

## AUTHOR CONTRIBUTIONS

Conception and design of study: Shengnan Lin, Xijun Pan, Ting-An Zhang. Acquisition of data: Shengnan Lin. Analysis and/or interpretation of data: Shengnan Lin,. Drafting the manuscript: Shengnan Lin, Deliang Meng. Critical revision: Shengnan Lin.

## DECLARATION OF COMPETING INTEREST

The authors declare that they have no known competing financial interests or personal relationships that could have appeared to influence the work reported in this paper.

## ACKNOWLEDGEMENTS

This work was supported by National Natural Science Foundation of China (No. U1508217 and No. U1710257) and the Fundamental Research Funds for the Central Universities (No. N162505002).

## DATA AVAILABILITY STATEMENT

All relevant data are included in the paper or its Supplementary Information.

## REFERENCES


Aghazadeh, M., Dalvand, S. & Hosseinifard, M. 2014 Facile electrochemical synthesis of uniform $\beta$-$Co(OH)_2$ nanoplates for high performance supercapacitors. *Ceramics International* **40** (2), 3485–3493.

Apiratikul, R. & Pavasant, P. 2008 Batch and column studies of biosorption of heavy metals by *Caulerpa lentillifera*. *Bioresource Technology* **99** (8), 2766–2777.

Cavaco, S. A., Fernandes, S., Quina, M. M. & Ferreira, L. M. 2007 Removal of chromium from electroplating industry effluents by ion exchange resins. *Journal of Hazardous Materials* **144** (3), 634–638.

Chaturvedi, A., Duggan, J. N., Roberts, C. B. & Suzuki, T. 2015 Magnetic properties of $Co_3O_4$ nanoparticles fabricated by chemical synthesis. In *Magnetics Conference*. IEEE, pp. 1–1.

Chiu, K.-L. & Chen, W.-S. 2017 Recovery and separation of valuable metals from cathode materials of spent lithium-ion batteries (LIBs) by ion exchange. *Science of Advanced Materials* **9** (12), 2155–2160.

Dang, H. T., Narbaitz, R. M., Matsuura, T. & Rana, D. 2007 Performance evaluation of commercial and newly-developed ultrafiltration membranes: Surface analysis and fouling tests American Water Works Association – AWWA Annual Conference and Exposition, ACE 2007, pp. 602–616.

Foroutan, R., Esmaeili, H., Rishehri, S. D., Sadeghzadeh, F., Mirahmadi, S., Kosarifard, M. & Ramavandi, B. 2017 Zinc, nickel, and cobalt ions removal from aqueous solution and plating plant wastewater by modified *Aspergillus flavus* biomass: a dataset. *Data in Brief* **12**, 485–492.

Ghosh, D., Giri, S. & Das, C. K. 2013 Hydrothermal synthesis of platelet $\beta$-$Co(OH)_2$ and $Co_3O_4$: smart electrode material for energy storage application. *Environmental Progress & Sustainable Energy* **33** (3), 1059–1064.

He, T., Chen, D., Jiao, X., Wang, Y. & Duan, Y. 2005 Solubility-controlled synthesis of high-quality $Co_3O_4$ nanocrystals. *Chemistry of Materials* **17** (15), 4023–4030.

Joss, A., Zabczynski, S., Göbel, A., Hoffmann, B., Löffler, D., McArdell, C. S. & Siegrist, H. 2006 Biological degradation of pharmaceuticals in municipal wastewater treatment: proposing a classification scheme. *Water Research* **40** (8), 1686–1696.

Karate, V. D. & Marathe, K. V. 2008 Simultaneous removal of nickel and cobalt from aqueous stream by cross flow micellar enhanced ultrafiltration. *Journal of Hazardous Materials* **157** (2–3), 464–471.

Kitahata, H., Tadanaga, K., Minami, T., Fujimura, N. & Ito, T. 2000 Preparation and ferroelectric properties of $YMnO_3$ thin films with c-axis preferred orientation by the sol-gel method. *Journal of Sol-Gel Science and Technology* **19** (1–3), 589–593.

Lee, H. I., Jung, Y., Kim, S., Yoon, J. A., Kim, J. H., Hwang, J. S. & Kim, J. M. 2009 Preparation and application of chelating polymer–mesoporous carbon composite for copper-ion adsorption. *Carbon* **47** (4), 1043–1049.

Li, Y. D., Li, X. L., He, R. R., Zhu, J. & Deng, Z. X. 2002 Artificial lamellar mesostructures to $WS_2$ nanotubes. *Journal of the American Chemical Society* **124** (7), 1411–1416.

Liang, Y., Li, Y., Wang, H., Zhou, J., Wang, J., Regier, T. & Dai, H. 2011 $Co_3O_4$ nanocrystals on graphene as a synergistic catalyst for oxygen reduction reaction. *Nature Materials* **10** (10), 780–786.

Liao, M., Liu, Y., Hu, Z. & Yu, Q. 2013 Novel morphologic $Co_3O_4$ of flower-like hierarchical microspheres as electrode material for electrochemical capacitors. *Journal of Alloys & Compounds* **562**, 106–110.

Liao, Q., Li, N., Jin, S., Yang, G. & Wang, C. 2015 All-solid-state symmetric supercapacitor based on $Co_3O_4$ nanoparticles on vertically aligned graphene. *Acs Nano* **9** (5), 5310–5317.

Liu, G., Zhao, C., Liu, T., He, D. & Suo, H. 2018 Facile route to achieve book-like tricobalt tetraoxide microstructures on copper foam for high performance supercapacitor. *Materials Letters* **220**, 78–81.

Lou, X. W., Deng, D., Lee, J. Y., Feng, J. & Archer, L. A. 2007 Self-supported formation of needlelike $Co_3O_4$ nanotubes and their application as lithium-ion battery electrodes. *Advanced Materials* **20** (2), 258–262.

Maile, N. C., Patil, R. T., Shinde, S. K., Kim, D.-Y., Fulari, A. V., Lee, D. S. & Fulari, V. J. 2009 Facial growth of $Co(OH)_2$ nanoflakes on stainless steel for supercapacitors: effect of deposition potential. *Journal of Materials Science: Materials in Electronics* **30**, 5555–5566.

Meher, S. K. & Rao, G. R. 2011 Ultralayered $Co_3O_4$ for high-performance supercapacitor applications. *Journal of Physical Chemistry C* **115** (31), 15646–15654.

Metz, R., Dornseifer, F., Golembiewski, W., Wieland, A. & Markham, T. 2015 Membrane separation method. WO/2015/024805 [patent].

Narbaitz, R. M., Rana, D., Dang, H. T., Morrissette, J., Matsuura, T., Jasim, S. Y., Tabe, S. & Yang, P. 2013 Field testing of modified CA membranes to remove PPCP from drinking water, AMTA/AWWA Membrane Technology Conference and Exposition 2013, pp. 107–123.

Pacholski, C., Kornowski, A. & Weller, H. 2002 Self-assembly of ZnO: from nanodots to nanorods. *Angewandte Chemie International Edition* **41** (7), 1188–1191.

Pan, X. J., Dou, Z. H., Zhang, T. A., Meng, D. L. & Fan, Y. Y. 2020 Separation of metal ions and resource utilization of magnesium from saline lake brine by membrane electrolysis. *Separation and Purification Technology* **251**, 117316.

Takahashi, M. & Fine, M. E. 1972 Magnetic behavior of quenched and aged $CoFe_2O_4$[Single bond]$Co_3O_4$ alloys. *Journal of Applied Physics* **43** (10), 4205–4216.

Tong, X., Wu, D., Zhang, C., Lian, K., Xiong, D., Xu, S. & Chu, P. K. 2017 Three-dimensional tetsubo-like $Co(OH)_2$ nanorods on a microporous electrically conductive network as an efficient electroactive framework for the hydrogen evolution reaction. *Journal of Materials Chemistry A* **5** (6), 2629–2639. Tang.

Tüysüz, H., Comotti, M. & Schüth, F. 2008 Ordered mesoporous $Co_3O_4$ as highly active catalyst for low temperature CO-oxidation. *Chemical Communications* **34**, 4022.

Wang, L., Liu, X., Wang, X., Yang, X. & Lu, L. 2010 Preparation and electrochemical properties of mesoporous $Co_3O_4$ crater-like microspheres as supercapacitor electrode materials. *Current Applied Physics* **10** (6), 1422–1426.

Xia, X. H., Tu, J. P., Mai, Y. J., Wang, X. L., Gu, C. D. & Zhao, X. B. 2011 Self-supported hydrothermal synthesized hollow $Co_3O_4$ nanowire arrays with high supercapacitor capacitance. *Journal of Materials Chemistry* **21** (25), 9319–9325.

Xie, D., Li, C., Tang, R., Lv, Z., Ren, Y., Wei, C. & Feng, C. 2014 Ion-exchange membrane bioelectrochemical reactor for removal of nitrate in the biological effluent from a coking wastewater treatment plant. *Electrochemistry Communications* **46**, 99–102.

Xu, J., Gao, P. & Zhao, T. S. 2012 Non-precious $Co_3O_4$ nano-rod electrocatalyst for oxygen reduction reaction in anion-exchange membrane fuel cells. *Energy & Environmental Science* **5** (1), 5333–5339.

Yavuz, E., Tokalıoğlu, Ş., Şahan, H. & Patat, Ş. 2013 Ultralayered $Co_3O_4$ as a new adsorbent for preconcentration of Pb(II) from water, food, sediment and tobacco samples. *Talanta* **115**, 724–729.

Yoneda, M., Gotoh, K., Nakanishi, M., Fujii, T., Konishi, Y. & Nomura, T. 2019 Influence of cobalt source compounds on the color tone of cobalt blue inorganic pigment. *Journal of the Society of Powder Technology, Japan* **56** (8), 446–451.

Youssry, S. M., El-Hallag, I. S., Kumar, R., Kawamura, G., Matsuda, A. & El-Nahass, M. N. 2020 Synthesis of mesoporous $Co(OH)_2$ nanostructure film via electrochemical deposition using lyotropic liquid crystal template as improved electrode materials for supercapacitors application. *Journal of Electroanalytical Chemistry* **857**, 113728.

Yu, H. Q. 2013 Novel morphologic $Co_3O_4$ of flower-like hierarchical microspheres as electrode material for electrochemical capacitors. *Journal of Alloys and Compounds* **562**, 106–110.

First received 19 January 2021; accepted in revised form 7 March 2021. Available online 18 March 2021